Gliding Performance of 3-D Corrugated Dragonfly Wing with Spanwise Variation

Y.H. Chen and M. Skote*

School of Mechanical and Aerospace Engineering, Nanyang Technological University, 50 Nanyang Avenue, Singapore 639798

* Corresponding author, Tel: (+65) 67904271, Fax: (+65) 67904062,

E-mail: mskote@ntu.edu.sg.

Abstract

Computational fluid dynamics (CFD) analyses are conducted to evaluate the gliding performance of a three-dimensional (3-D) corrugated wing while considering variations in the corrugation pattern across the wing span. Comparisons with the smoothly profiled counterpart assess the overall effect of wing corrugation on the gliding performance of the 3-D dragonfly wing, with primary focus on the effect of three-dimensionality as compared to the 2-D model.

Earlier simulations of both 2-D and 3-D gliding corrugated wings showed oscillations on lift and drag, while in nature, such force fluctuation would be undesirable and unrealistic. In contrast, no non-realistic fluctuations are present in this simulation. The feature included here, which has been neglected in the earlier studies, namely the variation of leading edge orientation along the wing span, is the crucial detail for preventing such non-realistic oscillations.

Furthermore, strong spanwise flow occurs in the 3-D corrugated wing used in this study, which earlier models have been incapable to capture.

Keywords: CFD, dragonfly gliding, wing corrugation, 3-D corrugated wing, profiled aerofoil.

1. Introduction

Dragonflies are unique in the sense that their extreme manoeuvrability, low noise signature and gliding ability make them the perfect insect to replicate for Micro-Air Vehicles (MAVs) (Chen et al., 2013a). During gliding flight, the dragonfly elevates into the air using flapping flight, and remains aloft without requiring further energy expenditure. Thus the gliding feature of dragonflies is a much desirable advantage to incorporate into MAVs in terms of power-saving ability.

Often the insect wings were assumed to be one flat piece in both mechanical and computational studies of flight performance. However, morphological and structural studies of dragonfly wings have illustrated the corrugation in dragonfly wings, formed by folding the wing membranes into V-shape grooves (Newman and Wootton, 1986; Rees, 1975b; Sudo et al., 2000; Wootton, 1981, 1992; Wootton, 1995). The corrugated wing configuration reinforces wing stiffness in the spanwise direction by allocating the longitudinal veins at the extrema of the grooves and the chordwise cross veins between the longitudinal veins, while at the same time allowing torsion and enhancing the development of wing camber (Ennos, 1995; Kesel et al., 1998; Norberg, 1972). Furthermore, morphological studies have revealed clear evidence of variation in corrugation configurations in both spanwise and chordwise directions, namely, the corrugated wing changes in vein size and orientation along the wing span and chord (Kesel et al., 1998; May, 1991; Mingallon and Ramaswamy, 2011; Okamoto et al., 1996; Vargas et al., 2008; Wootton, 1992).

At first glance, the irregular geometry of the corrugated wing promises poor aerodynamic performance in terms of low lift and high drag. Surprisingly, both experimental and computational studies conducted on corrugated dragonfly wing models have shown consistently that the corrugations do not significantly increase drag during gliding (Hord and Lian, 2012; Kesel, 2000; Kim et al., 2009; Lian et al., 2014; Okamoto et al., 1996; Vargas et al., 2008; Wakeling and Ellington, 1997). The reduction in the overall drag of the irregular corrugation is due to the negative viscous drag produced by the recirculating fluids trapped inside the corrugation grooves (Obata and Sinohara, 2009; Vargas et al., 2008).

However, there are constant debates on the aerodynamic benefits of corrugations during gliding. Early experiments on the corrugated aerofoil (Kesel, 2000; Rees, 1975a) demonstrated that the corrugated wing has no more aerodynamic significance over its smoothed counterpart, the profiled aerofoil. These experiments were mostly conducted at a Reynolds number ($Re \sim 10^4$) which is one order of magnitude higher than that used by dragonflies ($Re \sim 10^3$). Experiments conducted at even higher Reynolds numbers, however, showed that the corrugated aerofoil has better aerodynamic performance in generating higher lift, and discouraging flow separation and aerofoil stall (Tamai et al., 2007). In passing we note that even turbulent flows can be strongly affected by corrugation in forms of grooves inducing spanwise flow, see (Skote, 2014) for further references on that topic.

On the other hand, past computational studies conducted over a range of angles of attack (0° ~ 40°) as well as Reynolds numbers ($10^2 \sim 10^4$), have led to conclusions with controversy. Some claimed that corrugated wings produced higher lift and comparable drag than that of its profiled counterparts (Kim et al., 2009; Vargas et al., 2008). Others argued that corrugated wings had no aerodynamic benefits and produced higher drag (Hord and Lian, 2012).

So far, most mechanical and computational studies of corrugated wings during gliding are limited to two-dimensional models (Hord and Lian, 2012; Kim et al., 2009; Lian et al., 2014; Obata and Sinohara, 2009; Vargas et al., 2008), despite that morphological studies have revealed the fact that the corrugation configuration changes in size and orientation along the wing span and chord (Kesel et al., 1998; May, 1991; Mingallon and Ramaswamy, 2011; Okamoto et al., 1996; Vargas et al., 2008; Wootton, 1992). In those cases for which finite three-dimensional (3D) wing models were used (Kesel, 2000; Okamoto et al., 1996; Rees, 1975a), only homogeneous wing geometry was taken into consideration. In other words, only a uniform corrugation configuration was used throughout the wing span, there was no change in model thickness or orientation of the leading edges in the spanwise direction. Such 3D wing models (wing sections) were unable to capture the effect of this spanwise variation on the overall wing performance.

Kesel (2000) considered the changes in the corrugation configuration along the spanwise direction, by conducting the experiments on three pleated wing sections with distinct configurations of the pleats, according to the cross-sections extracted from three different spanwise positions in a wing of an *Aeschna cyanea*. Despite the effort in recognizing the spanwise variation of the corrugation patterns, the experimental models with different configurations were tested separately. Such experiments would not be able to capture the 3-D effects of changes in corrugation, vein size and orientation of the leading edges along the wing span as in the real dragonfly wings.

Up to date, detailed 3-D corrugated wing models were only used in studying the structural benefits of the corrugated wings (Kesel et al., 1998; May, 1991). Such wing models excel in presenting the realistic 3-D wing profile, by taking into account the vein network as well as the flexibility of the wing materials. However, only finite element analysis on the structural aspect of the 3-D corrugated wing was considered, while the flight performance was not studied. It is not hard to imagine the massive computation time and power required to include the dynamic flow of the fluids around such detailed wing model, thus it might not be rational to perform dynamic analysis of a fully corrugated wing. Nevertheless, certain key configurations in corrugation should still be considered, such as, the change in vein size and orientation of the leading edges along the wing span.

In this study, the computational fluid dynamic (CFD) analyses are carried out to examine the gliding performance of 3-D corrugated wing, taken into account the change of the corrugated configuration along the wing span, especially the change of leading edges orientation at the nodus. The aim of this study is to understand the overall effect of wing corrugation on the gliding performance of the 3-D dragonfly wing, with primary focus on the three-dimensional effect of the 3-D wing model compared to the 2-D model.

2. Materials and methods

Two different wing models are used in the present study: (1) Profiled wing and (2) Corrugated wing. All wing models have the same projected planform area and mean chord length. Detailed virtual wing geometries are described in Sec. 2.1, followed by descriptions of computational domains, boundary conditions and numerical methods in Sec. 2.2.

2.1. Modelling of the virtual wings

All three wing models were created based on the hindwing of the dragonfly *Anax Parthenope Julius*, the same as those used in the gliding flight experiments by Okamoto and co-workers (1996). The reasons of using Okamoto's corrugation configuration rather than the more commonly used configurations from Kesel (2000) are: (1) The two configurations are very similar, almost identical at the first two pleads which are our primary interest in this paper; (2) The gliding flight experiment by Okamoto and co-workers (1996) has been performed using the actual 3-D dragonfly wings, which might provide us with more insights of the three-dimensionality of the wing; (3) The hindwing was chosen as it has a larger posterior area, as such it affects aerodynamic performance more (Nagai et al., 2009; Rival et al., 2011; Wakeling and Ellington, 1997) and can hence provide a clearer picture from the results obtained.

All the virtual wings (the planform views of the actual wing and corrugated virtual wing can be seen in Fig. 1(a) and the profiled virtual wings in Fig. 2(b)) had a mean chord length of 11.77 mm and a projected planform area of 612.45 mm^2 with an aspect ratio of 8.83, identical to the actual dragonfly wing used by Okamoto and co-workers (Okamoto et al., 1996). Furthermore, Fig. 1(b) illustrates the cross-sectional sketches of the corrugated virtual wing as compared to their corresponding cross-section images of the actual wing (Okamoto et al., 1996) at (i) 0.4*l*, (ii) 0.5*l* and (iii) 0.7*l*, respectively. Note that 0.4*l*, 0.5*l* and 0.7*l* indicate the positions at 40 %, 50 % and 70 % of wing length, respectively.

As seen from the cross-sectional images of Okamoto's (1996) *Anax Parthenope Julius* hindwing in Fig. 1b(i)–(iii), the corrugation is more pronounced at the leading edges, especially the grooves formed by the first four veins, namely, costa (*C*), subcosta (*Sc*), radius (*R*), and mediana 1 (*M1*). By looking at the images from left to right, it is shown that corrugations become less prominent towards the trailing edge; while looking at the images from top to bottom in Fig. 1(b)(i) – (iii), it is seen that the corrugations smooth out towards the wing tip. Along the chordwise direction, the corrugations formed near the trailing edge have much smaller amplitude than those near the leading edge (Rees, 1975b). Moreover, the less prominent corrugations are located at the posterior area of the wing, where the flow is well separated and small pleats have much less effect on the flow around the wing. Considering the complexity in building a 3-D wing with every single corrugation and the massive computation power required to run flow analysis around such detailed wing model, it seems logical to neglect the corrugations at the posterior parts of the wing and focus on the corrugations shown near the leading edges. As such, only the veins and grooves formed by the first four veins were replicated in the corrugated virtual wing, whereas the posterior region towards the trailing edge was approximated as a single membrane with a uniform thickness of 0.02 % mean chord length (Kesel et al., 1998).

Morphological studies on the corrugation of dragonfly wings (Kesel, 2000; Okamoto et al., 1996; Rees, 1975b; Wootton, 1979) have shown that the foremost groove formed by the costa (*C*), subcosta (*Sc*) and radius (*R*) shows an upwards V-shape, extending spanwisely from the wing root up to the nodus. At the nodus, the subcosta fuses with the costa, causing an inverse of the most forward groove to face downwards, forming an inverted-V-shape groove after the nodus till the wing tip (refer to Fig. 1(a)(i) and Fig. 1(b)). Note that the above mentioned inversion of the V-shape groove formed by the four foremost leading edge veins is referred hereafter as the change in the orientation of the leading edges at the nodus. The cross-sectional sketches of the corrugated virtual wing shown in Fig. 1(b)(i) and (ii) demonstrate that our model captures the change in the orientation of the leading edges before and after the nodus.

Furthermore, the dimensions of the cross-sections of the veins and membrane were obtained via a scanning electron microscope (SEM S360, Leica) in an earlier study (Chen et al., 2013b). Fig. 1(a)(i)–(iii) shows the SEM images at the vicinity of the nodus and the cross-sections of the leading edge spar (costa) and the other veins (radius) respectively, providing us the bases in creating the 3-D vein-and-membrane structure of the corrugated virtual model.

Firstly, the virtual veins replicate the cross-sectional shapes depicted in Fig. 1(a)(ii) and (iii) of the actual dragonfly costa and radius veins. As such, the virtual leading edge spar (costa) is simplified as a rectangle of a shorter edge h and a longer edge w with a ratio of $h/w = 0.5$ as obtained from previous study (Chen et al., 2013b); while the other veins follow the geometry of the radius vein shown in Fig. 1(a)(iii) as an olival shape.

Secondly, the change in orientation of the leading edges before and after nodus is considered in the virtual corrugated model. The V-shape groove formed by the four foremost leading edge veins is flipped up into an inverted-V-shape groove at the nodus.

Lastly, the vein size reduction towards the wing tip (May, 1991) is taken into account in our geometry model, as shown in Fig. 1b(iii). As compared to the veins in Fig. 1b(ii), the sketch at the $0.7l$ position has similar shapes to the one at the $0.5l$ position, but in a smaller size, to reflect the tapering off of the wing towards the wing tip. In this case, the leading edge veins are reduced in size by up to half in the 0.7*l* position and by up to 75 % at the 0.85*l* position nearing the wing tip.

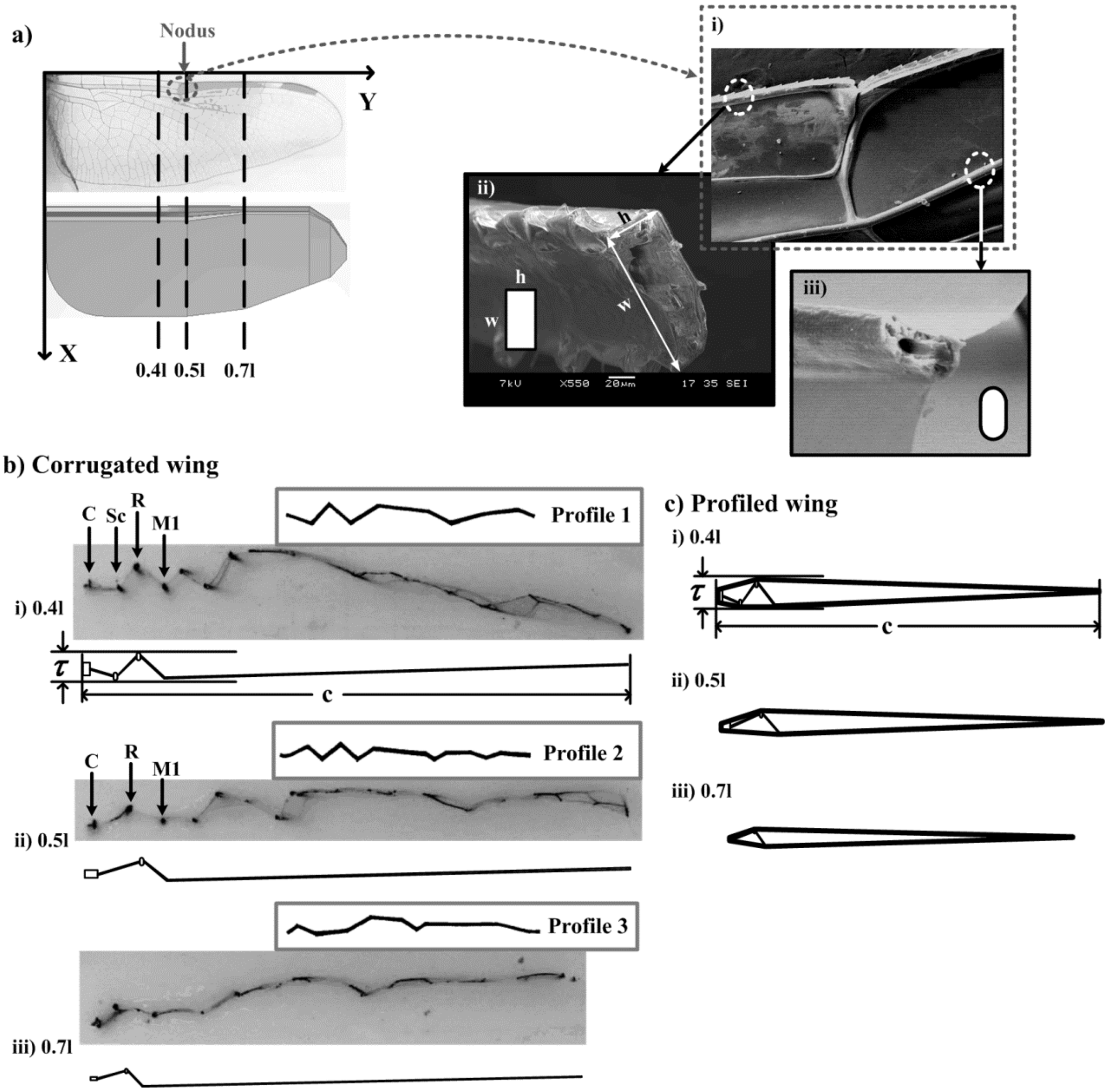

FIG.1. Geometry of the virtual wing models. (a) Plan view showing the planform of the corrugated virtual wing and its real counterpart, starting from top: image of actual *Anax Parthenope Julius* hindwing; image of virtual corrugated wing. Black dotted lines indicate 0.4*l*, 0.5*l* and 0.7*l* which correspond to 40 %, 50 % and 70 % of wing length. (i) SEM image of the nodus. (ii) SEM image of the cross-section of the leading edge spar (costa), with simplified rectangle representing its virtual counterpart. (iii) SEM image of the cross-section of other veins (radius), with approximated olival shape for its virtual counterpart. (b) Sketches of the cross-sections of the corrugated virtual wing compared to their corresponding images of the actual wing (Okamoto et al., 1996) and the sketches of Profile 1 to 3 of Kesel (2000) at (i) 0.4*l*, (ii) 0.5*l* and (iii) 0.7*l*, respectively. The naming of the first four veins is labelled as *C*, *Sc*, *R* and *M1* for costa, subcosta, radius and mediana 1, respectively. Sketches of veins are enlarged for clarity. As such, they are not drawn to scale, whereas the profile thickness, τ and the chord length, *c* of the cross-sections are drawn to scale. (c) Sketches of the cross-sections of the profiled virtual wings positioned at (i) 0.4*l*, (ii) 0.5*l* and (iii) 0.7*l*, respectively.

As demonstrated in Fig. 1(c), the profiled wing model was obtained by connecting the local extrema of the corrugated wing, creating an envelope around the corrugated wing as if the grooves were filled to form a streamlined structure. Both corrugated and profiled wings had a τ/c ratio of 6 %, 5 % and 5 % at 0.4l, 0.5l and 0.7l respectively, where τ is the profiled thickness and c is the chord length as shown in Fig. 1(b) and (c). The τ/c ratios at these spanwise positions are in accordance with the actual wings taken by Okamoto and co-workers (1996).

2.2. Computational domain and boundary conditions

In this study, ANSYS Workbench 14.0 was used to create the wing models, meshing and solving the continuity and momentum equations of an incompressible fluid. The same computational domain was applied to both wing models. The geometry models were subsequently meshed using tetrahedral elements to give a total of 1.06 million and 3.45 million volume cells around the profiled and corrugated wing, respectively. The grids were meshed so as to ensure that they were more clustered around the corrugations and towards the tips and edges of the wing, but coarser as they moved into the fluids, as shown in Fig. 2(a), (c) and (d). These set-ups were done to ensure that the viscous flow at the leading edge corrugations, trailing edges and the wing tip would be captured at a higher resolution and in greater accuracy and detail. In addition, the computational time was reduced if non-uniform grids were used. In Fig. 2(b), the planform views of the meshed wings illustrate that both wing models have the same mean chord length and projected planform area.

The overall computational domain shown in Fig. 2(a) was based on the symmetrical half of a spherical fluid enclosure with a radius of up to six chord lengths away from the wing root, which was done to avoid the unstable reflection of the solution at the fluid boundary (Weis-Fogh, 1973). The plan of symmetry was not located at the wing root, but at the midline of the insect thorax with a 2-mm distance from the wing root, the same as in the actual dragonfly.

As illustrated in Fig. 2(a), the surface boundary of the fluid enclosure was set as the velocity inlet, with free stream conditions applied. The velocity in the X-direction was set to 2.6 m/s, and 0 m/s in the other directions, to ensure that the analysis was carried out with the wing gliding forward in the negative X-direction. The velocity in the X-direction was obtained from the dragonfly's gliding speed (Wakeling and Ellington, 1997). Moreover, impermeable and no-slip wall conditions were applied at the interface between the wing and the fluid. At the plane of symmetry, flow symmetry conditions were applied.

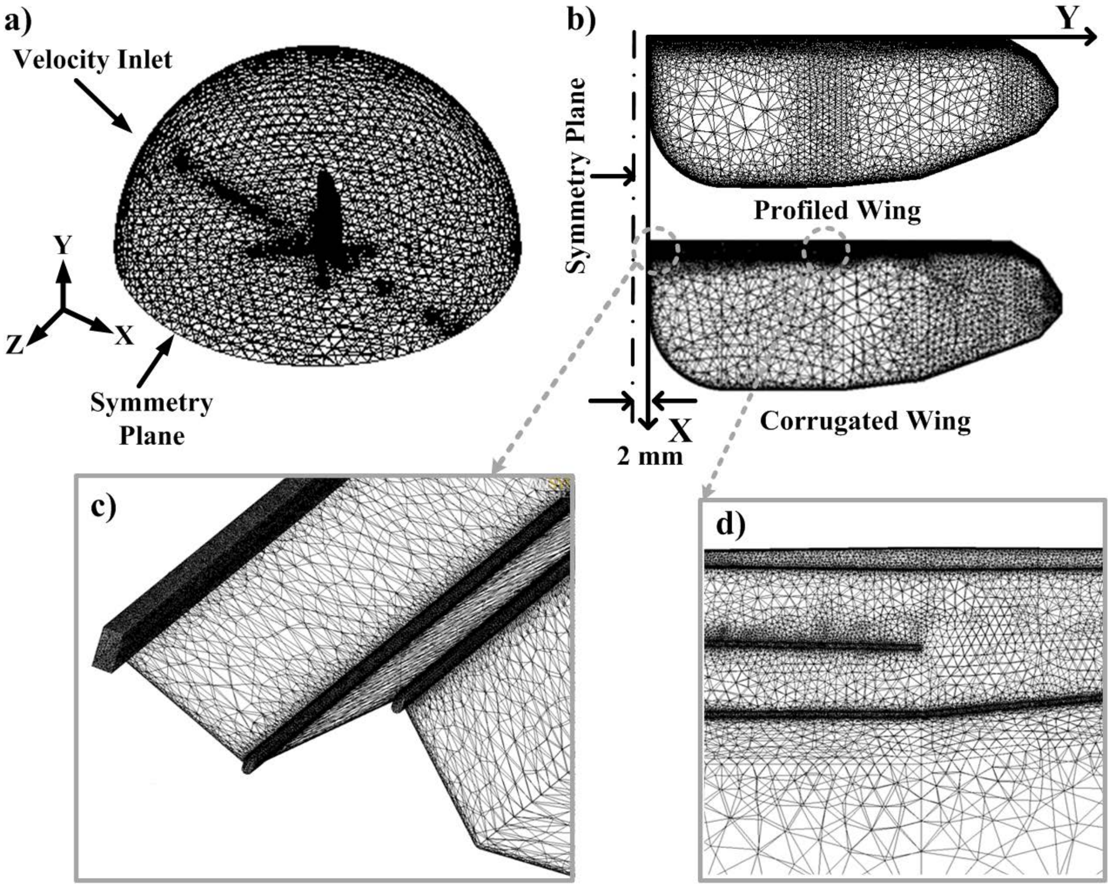

FIG.2. Computational domain and mesh for the virtual wings. (a) The semi-spherical computational domain. (b) Planform view of the virtual profiled and corrugated wing, with the surface meshes. The grids were meshed in a way that they were more clustered near the corrugations, tips and edges of the wing. The symmetry plane lies at the midline of the insect thorax, which is 2 mm away from the wing root. (c) Close-up view of the mesh at the corrugated leading edges. The mesh is finer over the veins as compared to the membranes. (d) Close-up view of the mesh about the nodus. The grids are more clustered near the leading edges, and gradually increasing in size as they moved away to the centre of the wing. It is also shown that the number of veins reduced from 3 to 2 after the nodus, causing an inverted-V-shape groove after the nodus.

In this study, the steady incompressible Navier-Stokes equations were solved using ANSYS FLUENT. The Reynolds number (*Re*) at which the simulations were performed can be calculated by:

$$Re = \frac{U_{ref} L_{ref}}{\nu}, \tag{1}$$

where v is the kinematic viscosity of air; L_{ref} is the reference length of the mean chord length; and U_{ref} is the free stream air velocity. Here, *Re* was approximated at 1400, similar to the typical *Re* values used in dragonfly gliding (Dickinson and Gotz, 1993; Kim et al., 2009; Lan and Sun, 2001; Wang et al., 2004). Moreover, an analysis of *Re* = 10000 was carried out to allow comparison with the past experiments (Kesel, 2000; Okamoto et al., 1996). Furthermore, a range of angle of attack (α = 0°, 5°, 10°, 40°) was analysed for insight of the influence of the angle of attack on the aerodynamic performance of the wing.

The key quantities to examine in this study are the lift coefficient C_l and the drag coefficient C_d defined as:

$$C_l = \frac{L}{0.5\rho U_{ref}^{\ 2} A_{ref}}, \tag{2}$$

and

$$C_d = \frac{D}{0.5\rho U_{ref}^{\ 2} A_{ref}}, \tag{3}$$

where L, D and P stand for the lift, drag and pressure acting on the wing, respectively; U_{ref} indicates the reference velocity, A_{ref}, the reference area, and ρ, the air density.

For the solution method, the pressure-velocity coupling was accomplished via the SIMPLE algorithm with the second-order upwind spatial discretization. For the time intervals, different values were used for the two Reynolds numbers: 1×10^{-4} s for *Re* = 1400 and 1×10^{-5} s for *Re* = 10000. For the convergence criteria, the residuals of continuity and velocities had to be reduced more than three orders of magnitude in each time step.

3. Results and Discussion

The grid sensitivity test is conducted for the present corrugated wing model to ensure the accuracy of the simulations in Sec. 3.1. Comparisons with past experimental studies are presented and discussed in Sec. 3.2. Moreover, the effect of wing corrugation on the overall gliding performance of the dragonfly wing is discussed in Sec. 3.3. Furthermore, Sec. 3.4 consist the primary analysis in this study, focusing on the three-dimensional effect of the spanwise changes of the corrugation configurations.

3.1. Grid sensitivity analysis

The resolution of the grids around the wing is particularly important as it determines the accuracy of the analysis. The size of the first grid that comes in contact with the wing (minimum grid size) was determined as 1 % of the boundary layer thickness at the wing trailing edge (Kim et al., 2009; Liu and Kawachi, 1998). The numerical solver was then tested with a further grid refinement at Re = 10000 and α = 5° to ensure the current grid size had enough resolution for this study. The minimum grid size in the refined case was reduced to half of that used in the baseline case. The resultant lift and drag coefficients of the two cases only differs by less than 2 %, confirming that the grid refinement did not significantly affect the simulation results. Therefore, the baseline case setting of the grid size was adapted in the present simulations.

3.2. Comparisons with past experiments

The gliding performance of the corrugated wing model was first evaluated at Re = 10000 to compare with the past experiments done by Okamoto *et al* (1996) and Kesel (2000). Both of these experiments were carried out using 3-D structures, with reinforced real dragonfly wings in the former study and remade thin brass mechanical wings in the latter. Three corrugation configurations were used in Kesel's experiments: (1) Profile 1 starting with a V-shape leading edge pleat, (2) Profile 2 with a horizontal leading edge, and (3) Profile 3 with an inverted-V-shape leading edge pleat, as illustrated earlier in Fig. 1(b). The computed lift and drag coefficients over various angles of attack were then compared with the experimental results in Fig. 3. In our evaluation, we used a similar approach to this higher Re flow as Kim *et al* (2009) and Vargas *et al* (2008).

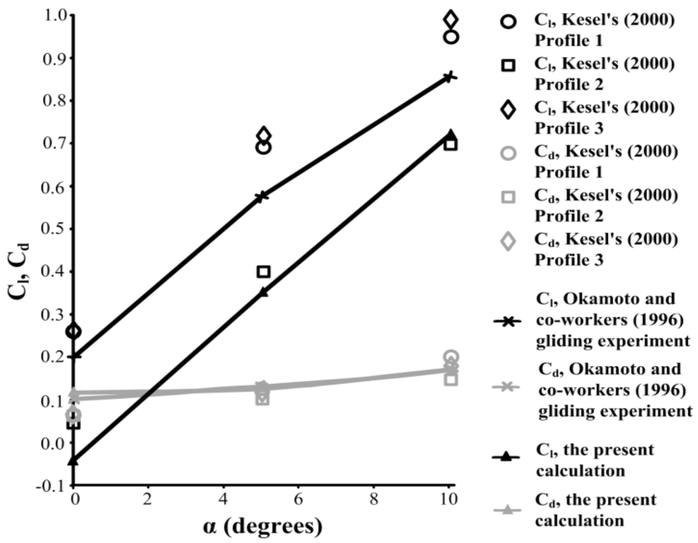

FIG.3. Comparison between the computed and the experimental force coefficients at *Re* = 10000 over various angles of attack.

As seen in Fig. 3, the drag coefficient of the present calculation shows good agreement with that of the experiments. Though there are discrepancies in the lift coefficients between the computed and experimental results, the results of the present calculation is nevertheless closer to the results obtained from Kesel’s Profile 2 wing model (2000), especially at α = 10° (margin of error less than 2 %). The computed corrugated wing model was built with an overall 3-D structure incorporating the orientation changes at the leading edges, whereas the wing models used in Kesel’s experiments were made into three separate wing sections with different corrugation configurations and tested individually. As such, differences in the resultant force coefficients are expected. On the other hand, the lift coefficients of the experiments done by Okamoto *et al* (1996) are considerably higher than our computed results, but the rate of lift coefficient increment over the change of angle of attack is very similar, especially within the smaller angle of attack region.

Furthermore, the flow field around the corrugated wing is compared with flow visualizations done by other researchers experimentally and numerically, to serve as further validation of the present numerical model. Since most of the past visualizations available up to day were done in a 2-D sense, the chordwise flow fields of the present 3-D model at different spanwise positions were compared with various 2-D studies at similar spanwise positions for validation (Obata and Sinohara, 2009; Vargas et al., 2008).

As shown in Fig. 4, the chordwise flow fields are adopted from the present computation and past flow visualizations at a Reynolds number of 10^3 and an angle of attack of 5° to the incoming flow. The surface streamlines of the chordwise planes show several similarities between our computed flows and those of other studies (Obata and Sinohara, 2009; Vargas et al., 2008). Firstly, as seen in Fig. 4(a) of the computed flows, the first pleat for dragonfly wings at 75 % of wing length are more or less horizontal, which leads to a lack of recirculation zone under the first pleat. Similarly, the flow visualization by Obata and Sinohara (2009) at the same wing span position illustrated no trapped vortex in the first groove, as shown in Fig. 4(b). Moreover, a recirculation zone is located after the first pleat as highlighted in Fig. 4(a)(i) of the computed flow, as well as in the flow visualization by Obata and Sinohara (2009) in Fig. 4(b).

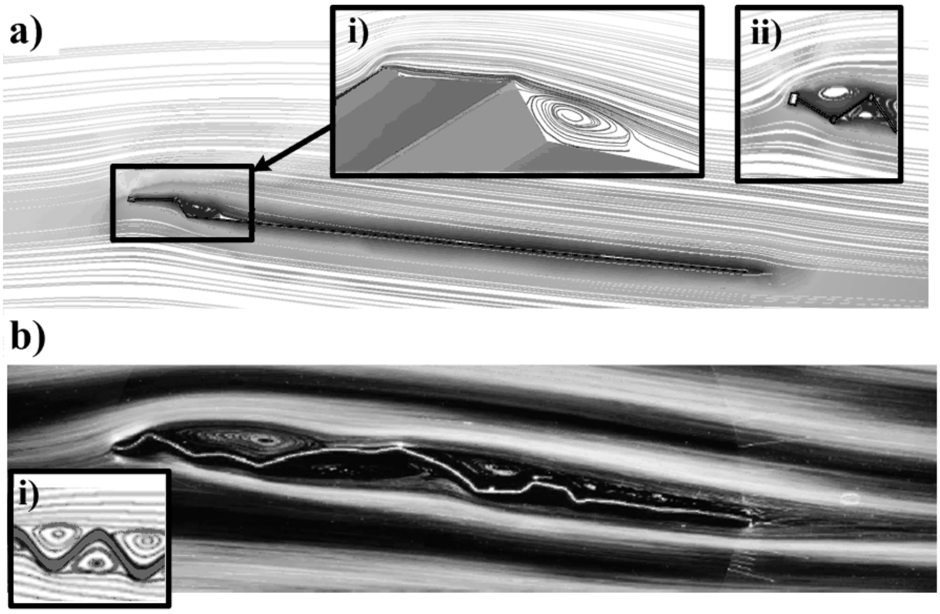

FIG.4. Comparison between the computed flow fields and the flow visualisations of other researchers. (a) Surface streamline of the computed corrugated wing at 75 % wing length, with (i) close-up view of the recirculation zone after the horizontal leading edge, and (ii) the vortices in each V-shape groove. (b) Flow visualized at 75 % wing length of the mechanical corrugated wing model from Obata and Sinohara (2009). The insert (i) demonstrates the vortices in the grooves of the computed flows from Vargas *et al* (2008).

Secondly, Fig. 4(a)(ii) emphasise the recirculating flows in all the V-shape grooves at 40 % of wing length of the present computation. The presence of the trapped vortex in each groove is in line with the past studies shown in Fig. 4(b)(i), which is demonstrated by the computed flows of a similar wing section of Vargas *et al* (2008).

The similarities between the surface streamlines of chordwise planes in the present computation and the 2-D flow fields in the other studies demonstrates the capability of the present simulation to capture the flow details around and within the grooves of the wing. From the above assessment of the computed results, together with the grid refinement analysis in Sec. 3.1, we are confident that the present simulation can capture the aerodynamic forces and flows of the 3-D corrugated dragonfly wings with reasonable accuracy. However, the 2-D force and flow analyses neither reflect the three-dimensionality of the flow along the spanwise direction of the actual dragonfly wings, nor accurately capture the overall performance of the corrugated wing. Thus, the analysis hereafter are conducted on the overall performance of the 3-D corrugated wing at low and high Reynolds numbers (*Re* = 1400 and *Re* = 10000) over a range of angles of attack (α = 0°, 5°, 10°, 40°), with primary focus on the three-dimensionality effect of the corrugated wing.

3.3. Overall performance of the corrugated wing

In this section, the 3-D corrugated wing is compared with the 3-D profiled wing. The overall performance of the corrugated wing is very similar to its profiled counterpart at *Re* = 1400, with the corrugated wing performing better at α = 5°, whereas the profiled wing performs better at α = 10°. As seen in Fig. 5, a decline of gliding performance occurs when the angle of attack is beyond 10° at *Re* = 1400. However, as the Reynolds number increases to 10000, the gliding ratio starts to drop once the angle of attack is beyond 5°. Even though the profiled wing shows better performance than that of the corrugated wing over all the angles of attack at *Re* = 10000, the decline in its gliding ability is more severe as indicated by the steeper descending slope between α = 5° and 10° in Fig. 5.

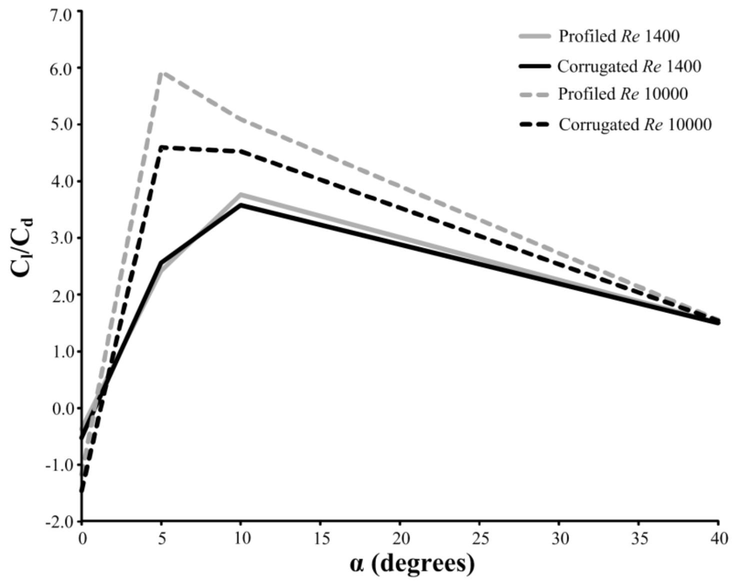

FIG. 5. Gliding ratio C_l/C_d of the corrugated and profiled wing at *Re* = 1400 and 10000 represented by solid and dotted lines, respectively.

A higher lift-to-drag ratio results in superior climb performance whilst reducing the amount of energy required to generate such climb. With the Reynolds number of 1400, the corrugated wing has a lift-to-drag ratio 6 % higher than that of the profiled wing at α = 5°. At this angle of attack, the lift coefficient C_l of the corrugated wing is comparable to that of the profiled wing, whereas the drag coefficient C_d is 7 % lower than that of the profiled wing. As the angle of attack increases to 10°, the profiled wing performs better than the corrugated wing in terms of a comparable lift but a 3 % lower drag. Both lift and drag values of the corrugated and profiled wings are comparable at α = 40°. As the Reynolds number increases to 10000, the gliding performance of the profiled wing is better than that of the corrugated wing over all the angles of attack examined.

In Fig. 6, the cross-sectional views of the streamlines are plotted on the vertical plane at 40 % of wing length, where the corrugation configuration is most pronounced. The above-mentioned trends of gliding performance of the two different wings can be well reasoned from the flow structures around the wings as illustrated in Fig. 6. It has been shown in earlier studies that the rotating vortices within the grooves of the corrugations and above the wing surface create a virtual profile around the wing, so that the wing acts as a thick smooth wing (Hord and Lian, 2012; Rees, 1975a; Vargas et al., 2008). In this study, the cyan-colour region around the wing shown in Fig. 6 indicates the virtual profile of the wing. The streamlines around the profiled and the corrugated wing are examined about three different angle of attacks (α = 5°, 10°, 40°) at Re = 1400 and 10000, respectively. As seen in Fig. 6(a) at Re = 1400, the profiled wing does not show any virtual profile thickness at low angles of attack (α = 5° and 10°), whereas the corrugated wing shows considerable virtual profile thickness at α = 10° but none at α = 5°.

At α = 5°, the flows around the profiled wing and corrugated wing are mostly identical, except the trapped vortex in each groove of the corrugated wing (see Fig. 6(a)(ii) inserted views of the grooves). The total drag acting on the wing consists of the viscous drag and the pressure drag. As seen in Fig. 6(a) at α = 5°, the flows remain attached to the surfaces of both wings, thus, the pressure drag is about the same for both wings. However, the recirculating flow in the grooves of the corrugated wing produces negative viscous drag so that the total drag of the corrugated wing becomes smaller than that of the profiled wing. At α = 5°, both wings produce similar total lift while the total drag of the corrugated wing is smaller, resulting in a higher lift-to-drag ratio than that of the profiled wing.

As the angle of attack increases to α = 10°, the virtual profile thickness of the corrugated wing increases, hence, the pressure drag also increases. At α = 10°, the virtual profile thickness of the corrugated wing is much higher than that of the profiled wing as shown from the cyan-colour flow region around the wing in Fig. 6(a). Therefore, the corrugated wing experiences much higher pressure drag than its profiled counterpart. The rotating flow in the grooves of the corrugated wing still produces negative viscous drag. However, due to the large separated flow across the corrugated wing, the pressure drag has more dominating effect than the viscous drag. Thus, the overall drag acting on the corrugated wing becomes larger than that on its profiled counterpart, which leads to the higher lift-to-drag ratio of the profiled wing than that of the corrugated wing at α = 10°.

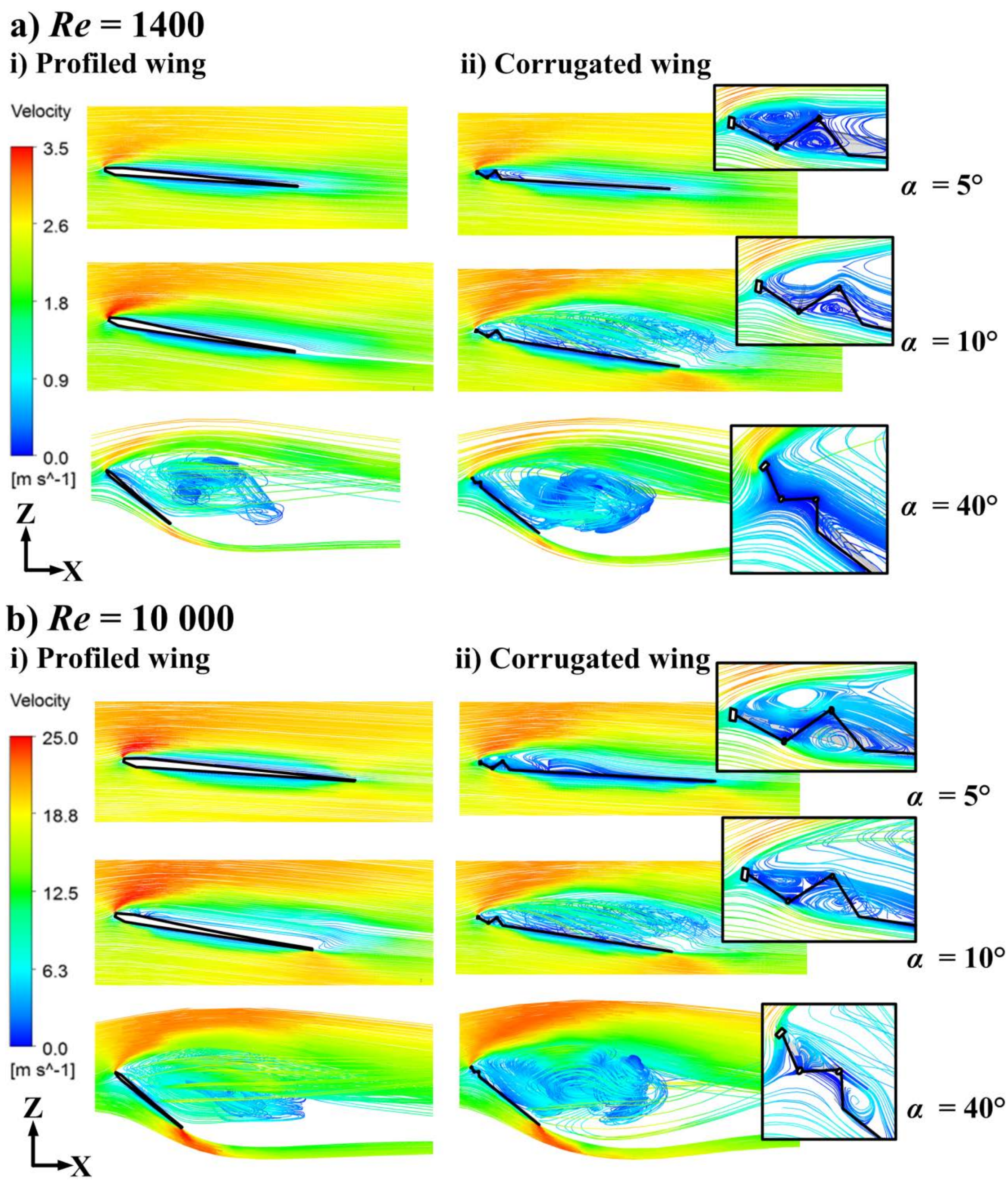

FIG. 6. Cross-sectional view of the streamlines on the vertical plane at 40 % of wing length at (a) *Re* = 1400 and (b) *Re* = 10000 for (i) the profiled and (ii) the corrugated wing, respectively.

When the Reynolds number increases to 10000, the virtual profile thickness also increases generally. At $\alpha = 5°$, visible virtual profile thickness is presented around the corrugated wing unlike its counterpart at *Re* = 1400, where no visible virtual profile thickness is observed. At *Re* = 10000 and $\alpha = 5°$, the trapped vortex in the grooves of the corrugated wing reduces the viscous drag, but the increase in the pressure drag is much larger due to the thicker virtual profile, resulting in an overall high drag than that of the profiled wing. Similarly, the thicker virtual profile around the corrugated wing at α = 10° causes the pressure drag of the corrugated wing to be higher than that of its profiled counterpart. These observations explain the lower gliding ratio of the corrugated wing compared to the profiled wing at *Re* = 10000 over the angle of attacks 5° and 10°.

On the other hand, at α = 40°, the flow is well separated and the wing corrugations have almost no effect on the flow field around the wing. Similarly, the Reynolds number has very small influence on the flow separation at such a high angle of attack. Thus, the gliding ratios of the two wings are mostly the same at α = 40° for both Reynolds numbers. Referring to the inserted close-up views of the grooves in Fig. 6, it is seen that the rotating flows are trapped in the grooves of the corrugated wings when the angle of attack is small. As the angle of attack increased to a large value of 40°, the flow is well separated from the wing surface, and no recirculating flows are found in the grooves of the corrugated wing. Hence, at α = 40°, the flow structures around the profiled and corrugated wing are similar, resulting in the overlapping gliding ratio shown in Fig. 5 for both wings and both Reynolds numbers.

3.4. 3-D effect of the corrugated wing

After the discussion of the overall performance of the corrugated wing over its profiled counterpart, we focus on the three-dimensionality of the present corrugated wing model in this section.

It is commonly reported in other studies that vortex shedding caused both lift and drag to oscillate on the wing sections (Hord and Lian, 2012; Kim et al., 2009; Lian et al., 2014; Vargas et al., 2008). These tested wing sections are either 2-D or 3-D but without changes of corrugation configurations along the wing span. According to these simulations, the dragonfly wings would be flattering during gliding, which seems hard to imagine in real dragonfly gliding. Naturally, the wing should remain stable in the sense that it does not flatter in the fluid during gliding.

In the present 3-D simulation, the oscillatory state is not attained as shown in Fig. 7(a), thus the wing does not flatter during gliding. In Fig. 7(b), the time history of the lift coefficients at *Re* = 1400 is demonstrated over a range of angles of attack examined by Kim and co-workers (Kim et al., 2009). The 2-D wing section that produced the oscillatory lift coefficients in Fig. 7(b) is adapted by Kim and co-workers (2009) from Profile 1 (see Fig. 1(b)(i)) of Kesel (2000), in which the corrugation is most strongly formed.

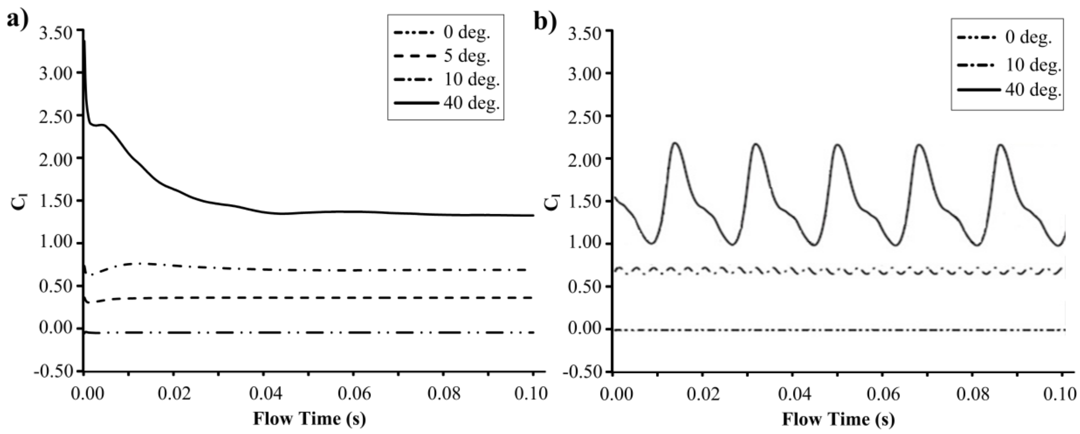

FIG.7. Comparisons of the time history of the lift coefficient between (a) the present 3-D corrugated wing calculation and (b) the 2-D corrugated Profile 1 simulation from Kim and co-workers (2009).

As seen in Fig. 7(b), the value of lift coefficient and the amplitude of oscillation increase as the angle of attack increases. At α = 0°, the lift coefficient of Kim *et al* (2009) has a constant value, which is similar to the constant lift coefficient obtained in the present study. Comparing the time history of the lift coefficients at angles of attack other than 0° in Fig. 7(a) and (b), it is shown that the constant lift coefficients of the present study have similar values as the mean values of the lift coefficients computed by Kim and co-workers (2009). For all angles of attack at *Re* = 1400 shown in Fig 7, the constant values of the lift coefficient obtained in the present 3-D study is slightly smaller than the mean values of the oscillatory lift coefficients calculated in the other 2-D computation (Kim et al., 2009).

To further assess the effect of three-dimensionality in the corrugated wing, the force coefficients of the present 3-D study and the three 2-D wing sections tested by Kim *et al* (2009) are plotted with respect to the angles of attack at *Re* = 1400. Referring to Fig. 8, it is shown that the force coefficients calculated by 2-D wing sections are generally higher than that of the 3-D wing. As seen in Fig. 8, the force coefficients of the 2-D wing sections are closer to the 3-D wing at lower angles of attack (α = 0 ~ 10°). As the angle of attack increases, the difference between the force coefficients increases dramatically as shown in Fig. 8 at α = 40°.

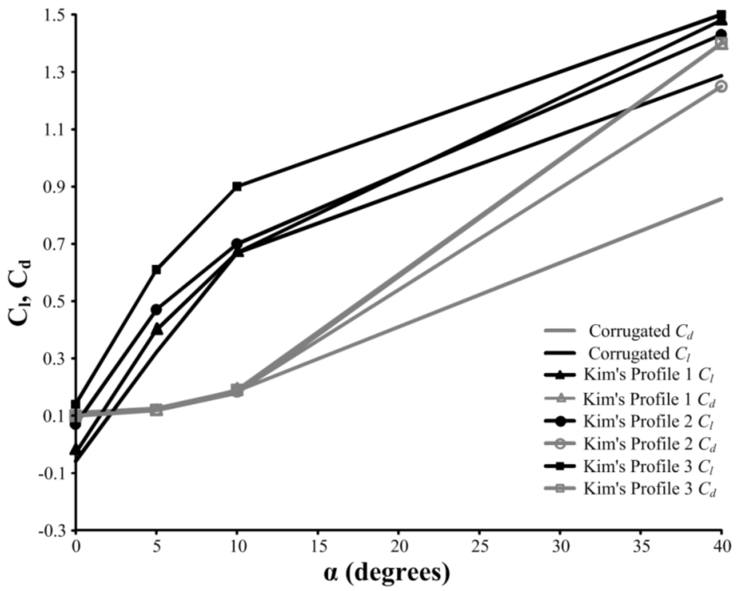

FIG.8. The force coefficients of the present 3-D corrugated wing and the three 2-D wing sections tested by Kim and co-workers (2009) plotted with respect to the angles of attack at *Re* = 1400. The lift and drag coefficients are plotted with various black and grey lines respectively.

Most of the past studies on the wing corrugation claimed that 2-D studies was sufficient as there was no velocity parallel to the wing span and no intrinsic three-dimensionality effects (Hord and Lian, 2012; Kesel, 2000; Kim et al., 2009; Okamoto et al., 1996; Vargas et al., 2008). However, it is noted that the so-called 3-D experiments or simulations were limited to wing sections, using only a uniform corrugation configuration throughout the wing span. Hence, there was no change in model thickness or leading edge orientation in the spanwise direction. Such limited 3D models cannot represent the entire wing, and were therefore unable to capture the effect of any spanwise variation on the overall wing performance.

In contrast, the computed corrugated wing model in this study was built with an overall 3-D structure incorporating the spanwise variations, especially the orientation changes of the leading edges. To assess the three-dimensionality of the corrugated wing, velocity streamlines are plotted on the vertical planes cutting the wing chordwisely along the wing span in Fig. 9. For earlier 2-D simulations, the velocity streamlines were contained within the cross-sectional plane, with no trace of spanwise flow (Hord and Lian, 2012; Kim et al., 2009; Vargas et al., 2008). However, as shown by the top views of the corrugated wing in Fig. 9, it is evidenced that the flow is three-dimensional in this 3-D study, with strong spanwise flow.

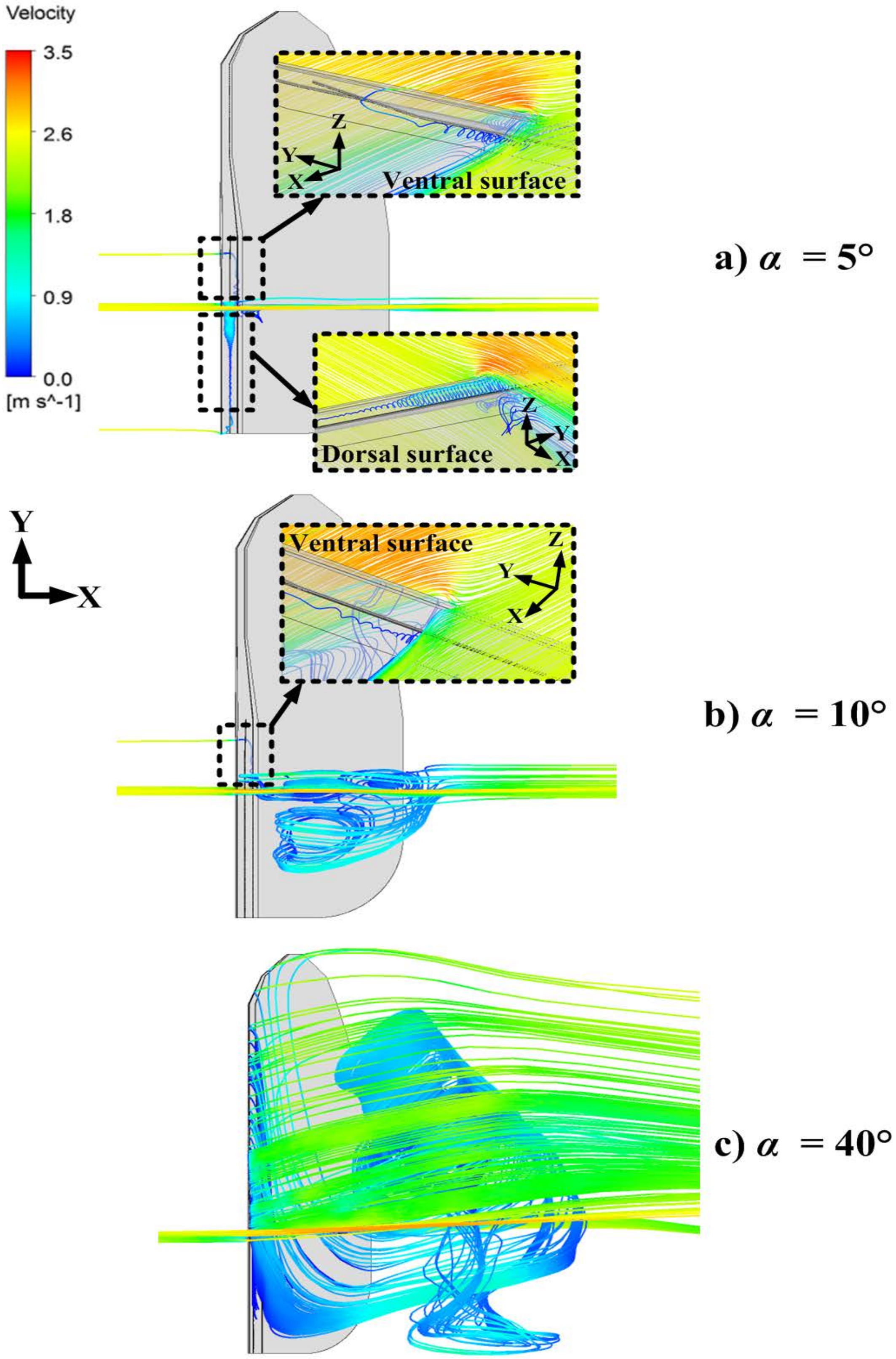

FIG.9. Top view of the velocity streamlines plotted on the vertical plane cutting the wing chordwisely at 40 % of wing length at Re = 1400 over the angles of attack (a) α = 5°, (b) α = 10° and (c) α = 40°. Inserted close-up views illustrate the conical flow in the first V-shape groove on the dorsal side of the wing and in the inverted-V-shape groove on the ventral side.

Figure 9 demonstrates the velocity streamlines at the *XY* vertical plane at 40 % of wing length over a range of angles of attack (α = 5 ~ 40°) at *Re* = 1400. Only streamlines originating upstream from the *Y* position of 40 % of wing length are plotted in Fig. 9, which is why the individual lines upstream conform into one single line, whereas, downstream of the wing, the streamlines have spread out very little in Fig. 9(a), moderately in Fig. 9(b), and are covering the whole wing in Fig. 9(c).

In Fig. 9, the velocity streamlines can be seen leaving the cross-sectional plane towards the wing root and tip in the spanwise direction for all the angles of attack. As shown in Fig. 9(a), the spanwise flow is mainly contained within the grooves of corrugations at α = 5°. The inserted close-up views in Fig. 9(a) illustrate the spanwise conical flow in the first V-shape groove on the dorsal side of the wing before the nodus as well as the spanwise flow in the inverted-V-shape groove on the ventral surface after the nodus. As the angle of attack increases, the spanwise flow becomes stronger and is no longer restricted to the grooves of corrugations. As seen in Fig. 9(b), the spanwise flow covers most of the wing chord at α = 10°, with a spanwise conical flow contained within the inverted-V-shape groove on the ventral side of the wing after the nodus. Such spanwise conical flows within the corrugated grooves are often missed out by other corrugated wing simulations. As seen in Fig. 9(a) and (b), the end of the conical flow goes backwards as a reversed flow in the negative *X* direction. Hence, if the simulation results only reflect the velocity streamlines in a forwards direction, the spanwise flow in the grooves will be overlooked, especially at lower angles of attack, where the spanwise flows only contain within the corrugation grooves. Moreover, the spanwise flow extends to the entire wing at α = 40° as shown in Fig. 9(c).

Hord and Lian (2012) have conducted studies on the suitability of a 2-D simulation for gliding corrugated wing. They tested a 3-D corrugated wing over a range of angles of attack from 0 to 12°, and concluded that there was no spanwise flow and the difference of force coefficients between the 2-D and 3-D cases were marginal. They further claimed that such difference in force coefficients obtained were merely due to the variation in grid generation between the 2-D and 3-D cases as there was no three-dimensionality effects of the corrugated wing (Hord and Lian, 2012). However, it is illustrated clearly in Fig. 9 of the present study that there exists spanwise flow in the 3-D corrugated wing. The main difference between Hord and Lian's 3-D model and that of the present simulation is the change in the orientation of the leading edges before and after the nodus. The corrugation configuration remained the same throughout the wing span in Hord and Lian's studies, whereas the reverse-V-shape groove formed by the first three leading edge veins flips up to V-shape groove after the nodus in the present model. We speculate that the spanwise variation, such as the changes in the orientation of the leading edges along the wing span, is the underlying cause of this spanwise flow.

To facilitate the visualization of the three-dimensional flow structure around the wing, the iso-surface of vorticity is plotted in Fig. 10 for the corrugated wing over a range of angles of attack (α = 5 ~ 40°) at Re = 1400. The overall iso-vorticity surface demonstrates the three-dimensional flow structure bound to the corrugated wing. The separation of the flow increases with the angle of attack as shown in Fig. 10(a) to (c). In Fig. 10(c), a 3-D vortex ring is formed by the leading edge and trailing edge vortices connected through the wing tip vortex. Such three-dimensionality of the flow structure is not readily reflected by 2-D vorticity contours done in earlier studies (Hord and Lian, 2012; Kim et al., 2009; Lian et al., 2014).

Moreover, close-up view at the V-shape grooves near the leading edges of the wing at α = 5° is inserted for Fig. 10(a). The close-up views of the iso-vorticity surface at the V-shape grooves are made with a transparency level of 0.6, so that the flow structures within the grooves can be observed. As shown in Fig. 10(a)(i) for the angle of attack 5°, the recirculating flows in the grooves are visible as darkened regions representing an inner vortex core region with the same vorticity magnitude as the overall iso-vorticity surface bound to the wing. For the case of α = 10°, similar recirculating flows are identified by the iso-vorticity surface within the grooves. However, such recirculating flow is absent at an angle of attack 40°. These observations are in accordance with the vorticity contours shown as insert (ii) in Fig. 10 and the velocity streamlines shown in Fig. 6(a) at an angle of attack 40°.

In addition, contours of the non-dimensional spanwise vorticity components are inserted as projections on the vertical plane at 40% wing length in Fig. 10(a) to (c) for better illustration. As demonstrated by insert (ii) in Fig. 10, the non-dimensional vorticity contours reflect the in-groove recirculating flows by showing more contour lines near to the wing surface (both basal and ventral) within the V-shape grooves, which is absent in the case of α = 40°.

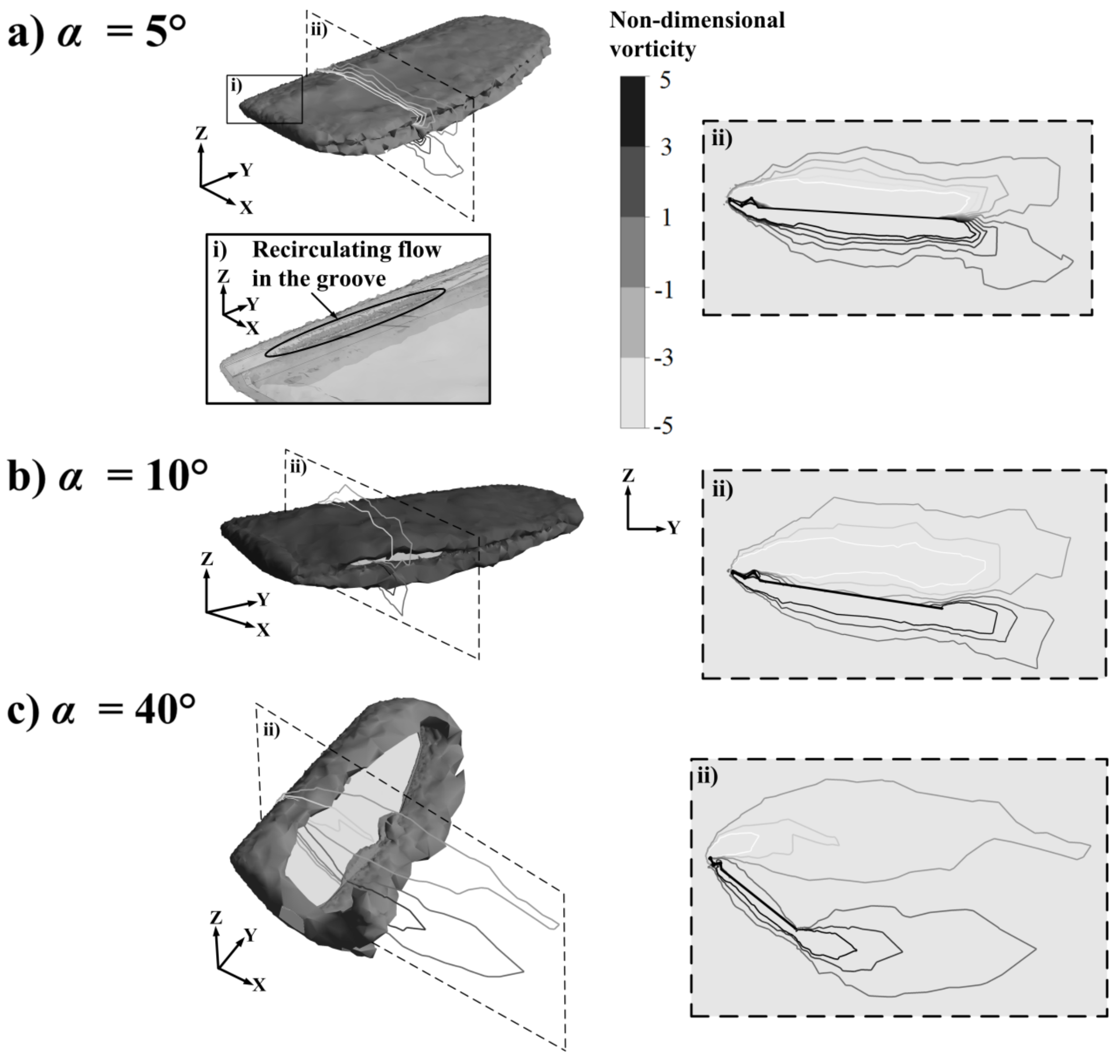

FIG. 10. Iso-surface of vorticity are plotted for the corrugated wing at *Re* = 1400 over the angles of attack (a) α = 5°, (b) α = 10° and (c) α = 40°. Inserted close-up views illustrate (i) Recirculating flows in the leading edge V-shape grooves of the corrugated wing; (ii) Contours of the non-dimensional spanwise vorticity components are plotted as projections on the vertical plane at 40% wing length.

These vorticity contours shows how the 3-D flow structures of the present study are reflected in two-dimensional views. They are similar to the vorticity contours plotted by other 2-D studies (Hord and Lian, 2012; Kim et al., 2009; Lian et al., 2014) in the sense that a pair of vortices is presented at the leading and trailing edges. However, the pair of vortices in other 2-D studies tends to leave the wing alternatively forming a von Karman vortex street, thus causing the force fluctuation detected in 2-D studies. In the present 3-D simulations, the contours of vorticity projection on the 2-D plane do not show the von Karman vortex street but two rather stable vortices at the leading and trailing edges, over the range of angles of attack.

Hence, the spanwise flow found in the present 3-D corrugated wing most likely stabilizes the vortex formed over the leading edges of the wing, by preventing it from accumulating into a large unstable vortex and shedding into the wake. Such stabilizing effect of the spanwise flow in preventing vortex shedding has been discussed in earlier studies (Chen and Skote, 2015; Sane, 2003). Thus, the vortex remains stable over the leading edges of the wing in the present 3-D simulation, and the vortex shedding which causes the oscillation on the 2-D aerofoils never occurs.

4. Conclusions

In conclusion, the corrugated wing performs best at $\alpha = 5°$ and $Re = 1400$ with a lift-to-drag ratio 6 % higher than that of the profiled wing. At this angle of attack, the corrugated wing has a comparable lift coefficient but 7 % smaller drag coefficient compared to the profiled wing. At this low angle of attack and Reynolds number, the rotating flow in the grooves of the corrugated wing produces significant negative viscous drag, which contributes to the small drag coefficients in the corrugated wing.

As the angle of attack and the Reynolds number increase, the profiled wing performs better than the corrugated wing in terms of a comparable lift but a lower drag. The rotating flow in the grooves of the corrugated wing still produces negative viscous drag. However, due to the large separated flow across the corrugated wing, the pressure drag exerts a more dominating effect than the viscous drag. Thus, the total drag acting on the corrugated wing becomes larger than that of the profiled wing.

Moreover, strong spanwise flow is presented in the present 3-D corrugated wing, indicating strong three-dimensionality of the corrugated wing model. Unlike the commonly reported oscillatory force coefficients of the 2-D simulations, the lift and drag coefficients do not oscillate in the present 3-D corrugated wing. This is a result of the three-dimensional effect of the corrugated wing. The spanwise flow found in the present 3-D corrugated wing stabilises the vortex formed over the leading edges of the wing, by preventing it from accumulating into a large unstable vortex and its shedding into the wake. Thus, the vortex remains stable over the leading edges of the wing, and the vortex shedding which causes the oscillation on the 2-D aerofoils never occurs in the present 3-D simulation. Hence, the present 3-D wing is more representative of the actual dragonfly gliding as naturally the wing should remain stable in the sense that it does not flatter during gliding. These specific attributes of the corrugated wing are exclusively shown in the present 3-D model with spanwise variation, which 2-D models and limited 3-D models are not able to capture.

Acknowledgments

Academic Research Fund Tier 1 (Grant No. RG95/13) from the Ministry of Education, Singapore, is greatly acknowledged.

References

Chen, Y. H. and Skote, M. (2015). Study of lift enhancing mechanisms via comparison of two distinct flapping patterns in the dragonfly Sympetrum flaveolum. Physics of Fluids 27, 033604.

Chen, Y. H., Skote, M., Zhao, Y. and Huang, W. M. (2013a). Dragonfly (Sympetrum flaveolum) flight: Kinematic measurement and modelling. Journal of Fluids and Structures 40, 115-126.

Chen, Y. H., Skote, M., Zhao, Y. and Huang, W. M. (2013b). Stiffness evaluation of the leading edge of the dragonfly wing via laser vibrometer. Materials Letters 97, 166-168.

Dickinson, M. H. and Gotz, K. G. (1993). Unsteady aerodynamic performance of model wings at low Reynolds numbers. Journal of Experimental Biology 174, 45-64.

Ennos, A. R. (1995). Mechanical Behaviour in Torsion of Insect Wings, Blades of Grass and other Cambered Structures. Proceedings of the Royal Society of London Series B: Biological Sciences 259, 15-18.

Hord, K. and Lian, Y. (2012). Numerical Investigation of the Aerodynamic and Structural Characteristics of a Corrugated Airfoil. Journal of Aircraft 49, 749-757.

Kesel, A. B. (2000). Aerodynamic Characteristics of Dragonfly Wing Sections Compared with Technical Aerofoils. Journal of Experimental Biology 203, 3125-3135.

Kesel, A. B., Philippi, U. and Nachtigall, W. (1998). Biomechanical Aspects of the Insect Wing: An Analysis Using the Finite Element Method. Computers in Biology and Medicine 28, 423-437.

Kim, W.-K., Ko, J. H., Park, H. C. and Byun, D. (2009). Effects of corrugation of the dragonfly wing on gliding performance. Journal of Theoretical Biology 260, 523-530.

Lan, S. L. and Sun, M. (2001). Aerodynamic properties of a wing performing unsteady rotational motions at low Reynolds number. Acta Mechanica 149, 135-147.

Lian, Y., Broering, T., Hord, K. and Prater, R. (2014). The characterization of tandem and corrugated wings. Progress in Aerospace Sciences 65, 41-69.

Liu, H. and Kawachi, K. (1998). A Numerical Study of Insect Flight. Journal of Computational Physics 146, 124-156.

May, M. L. (1991). Dragonfly Flight: Power Requirements at High Speed and Acceleration. Journal of Experimental Biology 158, 325-342.

Mingallon, M. and Ramaswamy, S. (2011). The architecture of the dragonfly wing: a study of the structural and fluid dynamic capabilities of the ansoptera's forewing. In: Proceedings of the ASME 2011 International Mechanical Engineering Congress & Exposition, IMECE2011, November 11-17, Denver, Colorado, USA.

Nagai, H., Nishi, A., Fujimoto, T. and Isogai, K. (2009). Study on flow interaction mechanism of fore- and hindwings of dragonfly. In: Proceedings of the 4th International Symposium on Aero Aqua Bio-Mechanisms, Shanghai, China.

Newman, D. J. S. and Wootton, R. J. (1986). An Approach to the Mechanics of Pleating in Dragonfly Wings. Journal of Experimental Biology 125, 361-372.

Norberg, R. A. (1972). The Pterostigma of Insect Wings an Inertial Regulator of Wing Pitch. Journal of Comparative Physiology 81, 9-22.

Obata, A. and Sinohara, S. (2009). Flow visualization study of the aerodynamics of modeled dragonfly wings. AIAA Journal 47, 3043-3047.

Okamoto, M., Yasuda, K. and Azuma, A. (1996). Aerodynamic Characteristics of the Wings and Body of A Dragonfly. Journal of Experimental Biology 199, 281-294.

Rees, C. J. C. (1975a). Aerodynamic properties of an insect wing section and a smooth aerofoil compared. Nature 258, 141-142.

Rees, C. J. C. (1975b). Form and function in corrugated insect wings. Nature 256, 200-203.

Rival, D., Schonweitz, D. and Tropea, C. (2011). Vortex interaction of tandem pitching and plunging plates: a two-dimensional model of hovering dragonfly-like flight. Bioinspiration & Biomimetics 6.

Sane, S. P. (2003). The aerodynamics of insect flight. Journal of Experimental Biology, 4191-4208.

Skote, M. (2014). Scaling of the velocity profile in strongly drag reduced turbulent flows over an oscillating wall. International Journal of Heat and Fluid Flow 50, 352-358.

Sudo, S., Tsuyuki, K. and Tani, J. (2000). Wing morphology of some insects. JSME International Journal Series C-Mechanical Systems, Machine Elements and Manufacturing 43, 895-900.

Tamai, M., Wang, Z., Rajagopalan, G., Hu, H. and He, G. (2007). Aerodynamic Performance of a Corrugated Dragonfly Airfoil Compared with Smooth Airfoils at Low Reynolds Numbers. In 45th AIAA Aerospace Sciences Meeting and Exhibit: American Institute of Aeronautics and Astronautics.

Vargas, A., Mittal, R. and Dong, H. (2008). A computational study of the aerodynamic performance of a dragonfly wing section in gliding flight. Bioinspiration & Biomimetics 3, 1-13.

Wakeling, J. M. and Ellington, C. P. (1997). Dragonfly flight. I. Gliding flight and steady-state aerodynamic forces. Journal of Experimental Biology 200, 543-556.

Wang, Z. J., Birch, J. M. and Dickinson, M. H. (2004). Unsteady forces and flows in low Reynolds number hovering flight: two-dimensional computations vs robotic wing experiments. Journal of Experimental Biology 207, 449-460.

Weis-Fogh, T. (1973). Quick estimates of flight fitness in hovering animals, including novel mechanisms for lift production. Journal of Experimental Biology 59, 169-230.

Wootton, R. J. (1979). Function, homology and terminology in insect wings. Systematic Entomology 4, 81-93.

Wootton, R. J. (1981). Support and deformability in insect wings. Journal of Zoology 193, 447-468.

Wootton, R. J. (1992). Functional morphology of insect wings. Annual Review of Entomology 37, 113-140.

Wootton, R. J. (1995). Geometry and Mechanics of Insect Hindwing Fans: A Modelling Approach. Proceedings of the Royal Society of London Series B: Biological Sciences 262, 181-187.